Spatially resolved simulation of a radio-frequency driven micro-atmospheric pressure plasma jet and its effluent

Torben Hemke, Alexander Wollny, Markus Gebhardt, Ralf Peter Brinkmann, Thomas Mussenbrock

Spatially resolved simulation of a radio frequency driven micro atmospheric pressure plasma jet and its effluent

Torben Hemke, Alexander Wollny, Markus Gebhardt,
Ralf Peter Brinkmann, and Thomas Mussenbrock
Department of Electrical Engineering and Information Sciences,
Ruhr University Bochum, D-44780 Bochum, Germany

(Dated: May 23, 2011)

Abstract

Radio frequency driven plasma jets are frequently employed as efficient plasma sources for surface modification and other processes at atmospheric pressure. The radio-frequency driven micro atmospheric pressure plasma jet (μAPPJ) is a particular variant of that concept whose geometry allows direct optical access. In this work, the characteristics of the μAPPJ operated with a helium-oxygen mixture and its interaction with a helium environment are studied by numerical simulation. The density and temperature of the electrons, as well as the concentration of all reactive species are studied both in the jet itself and in its effluent. It is found that the effluent is essentially free of charge carriers but contains a substantial amount of activated oxygen (O, O_3 and $O_2(^1\Delta)$). The simulation results are verified by comparison with experimental data.

I. INTRODUCTION

Microplasmas operated at atmospheric pressure have recently gained very high attention. A series of review papers and topical issues of leading scientific journals have discussed their technological promises as well as their scientific challenges [1–5]. A particularly popular class of microplasmas are radio-frequency driven plasma jets, originally proposed by Selwyn and co-workers in 1998 [6]. Many groups have investigated their prospect for surface modification; the studied processes include etching of tungsten, deposition and etching of silicon oxide, and cleaning of thermolabile surfaces from contaminants [7–12]. In order to improve the access for optical diagnostics, Schulz-von der Gathen and co-workers modified the originally axis-symmetric design of the jet to a plane-parallel geometry [13]. Their device, termed the micro atmospheric pressure plasma jet (μAPPJ), is depicted in Fig. 1. It is a geometrically and electrically symmetric capacitively coupled discharge driven via an impedance matching network by RF power of nominally 10 W at the frequency of 13.56 MHz. The plane-parallel stainless steel electrodes are 30 mm long, 1 mm wide, and separated by a gap of 1 – 2 mm. To allow direct optical access, the sides are made of quartz glass. The jet is operated with helium as the carrier gas and an admixture of oxygen at a relatively high flow rate of about 1 slm. The electron density is a few 10^{10} cm^{-3}, the ion densities are up to 10^{11} cm^{-3}, and the radical densities can reach several 10^{15} cm^{-3}.

This work expands earlier one-dimensional simulation approaches by Waskoenig et al. [14]. We study the μAPPJ by means of a two-dimensional numerical simulation. This allows us to study not only the discharge region but also the effluent of the jet which expands freely into the ambient atmosphere. In the effluent the gas is characterized by the absence of charged particles and a concentration of reactive radicals. It was found that the concentration of atomic oxygen decays only slowly outside the plasma volume and that the concentration of ozone even increases for a few centimeter. These phenomena have been found before by experiments [15–18]. (To show the reliability of the simulation results we present a comparison with experimental findings of Ellerweg et al. [18].)

II. DESCRIPTION OF THE NUMERICAL CODE

The simulations of this study are carried out with the fluid dynamics code *nonPDPSIM* designed and realized by Kushner and co-workers. For a detailed description of the code and its application to various types of plasmas and gas discharges, see the publications [19–22] and the citations therein. Here, we just briefly discuss the implemented equations and the underlying physics.

The code *nonPDPSIM* simulates the dynamics of weakly ionized plasmas in the regime of medium to high pressure. It takes into account the physics and chemistry of charged particles – electrons with mass m_e and charge $-e$, ions with mass m_j and charge q_j – and of the excited as well as the ground state neutrals (mass m_j). For all species j, the continuity equations (particle balances) are simultaneously solved, where $\vec{\Gamma}_j$ is the particle flux density and S_j the source and loss term, respectively:

$$\frac{\partial n_j}{\partial t} = -\nabla\cdot\vec{\Gamma}_j + S_j. \tag{1}$$

The fluxes are calculated from the momentum balances in the drift-diffusion approximation evaluated in the local center-of-mass system. D_j and μ_j are the diffusion constant and the mobility (if applicable) of the species j, $\vec{E}$ is the electrical field, and $\vec{v}$ is the mass-averaged advective velocity of the medium:

$$\vec{\Gamma}_j = n_j\vec{v} - D_j\nabla n_j + \frac{q_j}{|q_j|}\mu_j n_j\vec{E}. \tag{2}$$

For the electron fluid, additionally an energy balance equation is solved which takes into account Ohmic heating and the energy losses due to elastic and inelastic interaction with the neutrals and ions as well as heat conduction,

$$\frac{\partial}{\partial t}\left(\frac{3}{2}n_\mathrm{e}T_\mathrm{e}\right) = \vec{j}\cdot\vec{E} - \nabla\cdot\left(-\kappa_\mathrm{e}\nabla T_\mathrm{e} + \frac{5}{2}T_\mathrm{e}\vec{\Gamma}_\mathrm{e}\right) - n_\mathrm{e}\sum_i \Delta\epsilon_i k_i n_i. \tag{3}$$

To capture the non-Maxwellian behavior of the electrons, all electronic transport coefficients (the mobility μ_e, the diffusion constant D_e, and the thermal conductivity κ_e) as well as the electronic rate coefficients in eqs. (1) and (2) are calculated by the local mean energy method: A zero-dimensional Boltzmann equation for the electron energy distribution $f(\epsilon)$ and the transport and rate coefficients is solved for the locally applicable gas composition and various values of the electrical field. The tabulated data are then consulted in dependence of the fluid dynamically calculated electron temperature T_e.

The plasma equations are coupled to a modified version of the compressible Navier-Stokes equations which solve for the gas density ρ, the mean velocity $\vec{v}$, and the gas temperature T. Here, p is the scalar pressure, given by the ideal gas law, and $\overline{\overline{\tau}}$ the viscous stress tensor, related to the velocity shear via the viscosity. The contributions to the energy equation from Joule heating include only ion contributions; the heat transfer from the electrons is included as a collisional change in the enthalpy. The heat capacity and the thermal conductivity of the gas are c_p and κ, respectively, Δh_j denotes the enthalpy change due to reaction j:

$$\frac{\partial \rho}{\partial t} = -\nabla \cdot \rho \vec{v}, \tag{4}$$

$$\frac{\partial (\rho \vec{v})}{\partial t} = -\nabla p - \nabla \cdot \rho \vec{v}\vec{v} - \nabla \cdot \overline{\overline{\tau}} + \sum_i (q_i n_i - m_i \mu_i S_i)\vec{E}, \tag{5}$$

$$\frac{\partial (\rho c_\mathrm{p} T)}{\partial t} = -\nabla \cdot (-\kappa \nabla T + \rho \vec{v} c_p T) - p(\nabla \cdot \vec{v})(\overline{\overline{\tau}} \cdot \nabla \vec{v}) - \sum_j \Delta h_j S_j + \sum_i \vec{j}_i \cdot \vec{E}. \tag{6}$$

Finally, the potential Φ is calculated from Poisson's equation. (The code works in the electrostatic approximation so that $\vec{E} = -\nabla\Phi$.) The charge density on its right stems from the charged particles in the plasma domain and from the bound charges ρ_s at the surfaces. The coefficient $\varepsilon = \varepsilon_0 \varepsilon_\mathrm{r}$ represents the permittivity of the medium:

$$-\nabla \cdot (\varepsilon \nabla \Phi) = \sum_j q_j n_j + \rho_\mathrm{s}. \tag{7}$$

The surface charges are governed by a separate balance equation, where σ is the conductivity of the solid materials and the subscript s indicates evaluation on the surface:

$$\frac{\partial \rho_\mathrm{s}}{\partial t} = \left[\sum_j q_j (-\nabla \cdot \vec{\Gamma}_j + S_j) - \nabla \cdot (\sigma(-\nabla\Phi)) \right]_\mathrm{s}. \tag{8}$$

The dynamical equations are complemented by an appropriate set of boundary conditions. Electrically, the walls are either powered or grounded. With respect to the particle flow, they are either solid, or represent inlets or outlets: The flow is specified to a given flux, while the outlet flow is adjusted to maintain the pressure. Finally, it is worth mentioning that the actual implementation of the equations poses some difficulties due to the vast differences in the time scales of the dynamics of the plasma and the neutrals. These difficulties are overcome by the methods of time-slicing and subcycling.

III. THE DETAILS OF THE SIMULATION CASE

The described model is employed to simulate a μAPPJ, similar to the one depicted in Fig. 1. In our case, the electrodes are 30 mm long, their separation is 1.8 mm. The simulation resolves two Cartesian dimensions x and y. In direction z, translational invariance is assumed. (This assumption reflects a limitation of the code. We believe that the corresponding modeling error is not too severe; it is still possible to resolve the plasma distribution between the electrodes and the evolution along the direction of the gas flow. The main error of our "infinitely wide" model lies in the boundary conditions of the advective velocity of the fluid at the quartz boundaries. It translates into the coefficient of the Hagen-Poiseuille equation being off by about 60%, not too severe a problem as we control the total flux through the jet, not the pressure differential between and outlet.)

The simulation domain is depicted and explained in Fig. 2. The triangular unstructured mesh consists of approximately 10.000 nodes. 80% are located in the plasma domain including the effluent, their density is highest between the symmetrically powered RF electrodes. The outer boundary of the simulation domain is electrically grounded.

The device is operated as a helium-oxygen μAPPJ in a pure helium atmosphere at 10^5 Pa. The inlet is fed with a gas mixture with a high flow rate of 1 slm, corresponding to a maximum advective velocity of about 1500 cm/s. The mixing ratio of helium to oxygen is 1000 to 5; experiments indicate that these conditions maximize the concentration of atomic oxygen [15]. To maintain the outer environment, pure helium is injected at a flow rate of 1 slm at the left side of the simulation domain. The outlet is controlled to maintain a constant pressure. The following species are taken into account: Ground state neutrals O_2, O, O_3, and He, $O_2(\nu)$, representing the first four vibrational levels of O_2, the electronically excited states $O_2(^1\Delta)$, $O_2(^1\Sigma)$, $O(^1D)$, $O(^1S)$, and $He(^2S)$, positive ions O_2^+, O^+, and He^+, negative ions O_2^-, O^-, and O_3^-, and electrons. The reaction chemistry applied here is described in more detail in [21]. Following [23] we neglect ionized helium dimers He_2^+ and excimers He_2^*. It has been shown that these species (which require a high electron temperature) play a minor role when the discharge is dominated by the reactive oxygen species; this holds for mixtures with an O_2 content of 0.5 % or more. Finally, the secondary electron emission coefficient of the surfaces is set equal to 0.1.

IV. SIMULATION RESULTS

As a result of our simulations, we obtain a complete picture of the dynamics of the μAPPJ under certain conditions. In this manuscript we focus on phase-averaged quantities. The results correspond to a total RF power deposition in the plasma of 0.5 W. (This value is considerably lower than the nominal RF generator power of about 10 W of the corresponding experiments. The deviation can be explained by parasitic losses in the matching network and the feed cables. Order-of-magnitude differences between the generator power and the plasma heating power are also observed in other regimes [24, 25].)

Figs. 3 and 4 show the two-dimensional spatial distribution of the electron density n_e and the electron temperature T_e. The 1D profiles (normal to lateral gas flow) of the charged particle densities and the electron temperature at a position x=2 cm, are shown in Figs. 5 and 6. Between the electrodes we notice the typical structure of a capacitively coupled discharge. The plasma is separated in two distinct regions, the plasma bulk and the sheath. The maximum of the electron density is approximately 1.9×10^{10} cm^{-3}. In the sheaths it decreases to a much smaller value. A strongly electronegative characteristic can be observed. The charged particles are dominated by the oxygen species. The positive ion density is almost exclusively due to O_2^+; O^+ and He^+ are negligible. The negative ions are O_3^-, O_2^- and O^-, in descending order. The electron temperature T_e in the plasma bulk is approximately 2 eV, in the sheath region it is slightly larger due to increased Ohmic heating and possibly due to secondaries.

The effluent of the jet has the character of an afterglow. Both the electron density and the electron temperature drop abruptly. This can also be seen from the curves in Fig. 7 which show the distribution of the two quantities along the middle axis of the simulation. In the jet channel, n_e and T_e are almost constant; after the end of the electrodes (the beginning of the effluent) – indicated by the vertical dotted line – both quantities decay exponentially. Fig. 8 shows that this feature holds also for all other charged particles except for O_2^+ and O_3^-. We conclude from these results that the plasma dynamics in the jet is (with respect to the x-coordinate) "local". Generation of plasma is governed by the local electron temperature profile which in turn is a functional of the local field distribution; losses are dominated by drift and diffusion to the electrodes: The plasma chemistry is so "fast" that transport due to the flow plays a minor role and the solutions become essentially one-dimensional. The

agreement of our results with the results performed by Waskoenig et al. by means of a 1D-fluid model is thus not a coincidence [14].)

The picture changes drastically when we focus on the reactive neutral species. (See Fig. 9.) For the neutrals the chemistry is "slow", and it takes a considerable time (or distance along the flow) for the species to build up. Particularly O, O_3 and $O_2(^1\Delta)$ increase in the jet channel. In the effluent, their destruction is also slow; they are transported over a distance of a few cm. The density of ozone even increases slightly and remains constant for a certain length. The reason for this behavior is that the activated species are not directly generated by the plasma electrons but by heavy particle chemistry. A particular case are the ions O_2^+ and O_3^-. The generation of O_2^+ is via electron impact ionization and therefore fast, the generation of O_3^- is slow because it involves ion chemistry. The destruction is slow for both species, they are transported about 1 cm into the effluent: O_2^+ and O_3^- form the end points of the positive and negative ion chemistry, respectively, and their direct recombination constant is relatively small.

Further down in the effluent, therefore, only three species play a role: O, O_3 and $O_2(^1\Delta)$. Their spatial distribution is shown in Figs. 10, 11, and 12. Atomic oxygen reacts with molecular oxygen to ozone; its density thus decays exponentially. The rate constant, however, is relatively small; 2 cm behind the nozzle of the jet it still has a concentration of 3×10^{14} cm^{-3}. The densities of ozone (2×10^{15} cm^{-3}) and excited oxygen (1×10^{15} cm^{-3}) remain nearly constant up to the outlet.

An exhaustive comparison of our simulations with experimental data is currently underway and will be presented in the near future. Nonetheless, some preliminary results may be of interest: Fig. 13 shows the profiles of O and O_3 along the jet and the effluent, in comparison with experimental results obtained by Ellerweg et al. with quantitative molecular beam mass spectrometry and two-photon absorption laser-induced fluorescence spectroscopy [18]. We find that the simulation results are in excellent agreement with the experiment. (Note that we changed the simulation parameters slightly to accommodate the experiment: The jet gap size was decreased to 1 mm. The power deposition was kept constant and the temperature of the electrodes – a very sensitive parameter which controls the production of reactive oxygen species in the effluent – was set to 330 K.)

V. SUMMARY AND CONCLUSION

In this work we employed the code *nonPDPSIM* to conduct a numerical simulation of an RF-driven atmospheric pressure plasma jet operated with a mixture of helium and oxygen. In several aspects our study goes beyond previous work. The two-dimensional spatial resolution of the simulation allows to investigate not only the profile of the discharge parameters between the electrodes but also their transport through the jet and into the environment. We found a pronounced difference in the behavior of the charged particles and the neutrals. The charges – e and predominantly O_2^+, O^-, O_2^- – are governed by a "fast" chemistry: In the jet, their production is local in x and their losses are dominated by drift and diffusion to the electrodes – this can be understood in a 1d-picture which resolves only the y-axis [14]. In the effluent, they are virtually absent. The neutrals, in contrast, obey a "slow" chemistry. The reactive oxygen species O, O_3 and $O_2(^1\Delta)$ build up along the x-axis of the jet and are then flow-transported far into the effluent; their distribution is genuinely "two-dimensional". (Actually, it will be "three-dimensional". We believe, however, that the restriction of our analysis to two dimensions does not introduce more than quantitative errors.)

In summary, our simulation results indicate that the influence of the jet on the environment is primarily of chemical nature. Even in the jet, the density of the activated oxygen species is four orders of magnitude higher than the maximum density of the charges, and in the effluent the charges vanish completely. This view is in agreement with the experimental findings established by various other researchers [13–18, 26, 27]. In particular ozone with a longer lifetime than atomic oxygen and the very reactive $O_2(^1\Delta)$ are able to react with surfaces over a long distance [28]. Excited atomic oxygen species, in contrast, plays a relatively minor role due to its lower concentration.

Further work on the μAPPJ will focus on the transient behavior of the device and also on its interaction with a more complex environment. In particular, it is planned to investigate the effect of an atmosphere which consists of ambient air (instead of pure helium), and also the interaction of the effluent on a material substrate.

VI. ACKNOWLEDGMENT

The authors gratefully acknowledge fruitful discussions with Prof. M.J. Kushner and Dr. N.Y. Babaeva from the University of Michigan at Ann Arbor. Financial support by the Deutsche Forschungsgemeinschaft in the frame of Research Group 1123 *Physics of Microplasmas* is also acknowledged.

[1] H.W. Lee, G.Y. Park, Y.S. Seo, Y.H. Im, S.B. Shim, and H.J. Lee, *J. Phys. D: Appl. Phys* **44**, 053001 (2011)

[2] K.H. Becker, H. Kersten, J. Hopwood, J.L. Lopez, Eur. Phys. J. D **60**, 437439 (2010)

[3] M.G. Kong, G. Kroesen, G.E. Morfill, T. Nosenko, T. Shimizu, J. van Dijk, J.L. Zimmermann, New. J. Phys. **11**, 115012 (2009)

[4] K.H. Becker, U. Kogelschatz U, K.H. Schoenbach, R.J. Barker (ed) *Non-Equilibrium Air Plasmas at Atmospheric Pressure* (IOP Publ., Bristol, UK, 2004)

[5] K.H. Becker, K.H. Schoenbach, J.G. Eden, J. Phys. D: Appl. Phys **39**, R55 (2006)

[6] A. Schütze, J.Y. Jeong, S.E. Babayan, J. Park, G.S. Selwyn, R.F. Hicks, IEEE Trans. Plasma Sci. **26**, 1685 (1998)

[7] S.E. Babayan, J.Y. Jeong, V.J. Tu, J.Park, G.S. Selwyn, R.F. Hicks, Plasma Sources Sci. Technol. **7**, 286 (1998)

[8] H.W. Herrmann, I. Henins, J. Park, G.S. Selwyn Phys. Plasmas **6**, 2284 (1999)

[9] G.S. Selwyn, H.W. Herrmann, J. Park, I. Henins Contrib. Plasma Phys. **6**, 610 (2001)

[10] T. Ichiki, R. Tauro, Y. Horiike, J. Appl. Phys. **95**, 35 (2004)

[11] R.M. Sankaran, K.P. Giapis, J. Phys. D: Appl. Phys. **36**, 2914 (2003)

[12] V. Raballand, J. Benedikt, A. von Keudell, Appl. Phys. Lett. **92**, 091502 (2008)

[13] V. Schulz-von der Gathen, L. Schaper, N. Knake, S. Reuter, K. Niemi, J. Winter, J. Phys. D: Appl. Phys **41**, 194004 (2008)

[14] J. Waskoenig, K. Niemi, N. Knake, L.M. Graham, S. Reuter, V. Schulz-von der Gathen, T. Gans, Plasma Sources Sci. Technol. **101**, 123306 (2010)

[15] N. Knake, K. Niemi, S. Reuter, V. Schulz-von der Gathen, J. Winter, Appl. Phys. Lett **93**, 131503 (2008)

[16] N. Knake, S. Reuter, K. Niemi, V. Schulz-von der Gathen, J. Winter, J. Phys. D: Appl. Phys **41**, 194006 (2008)

[17] B. Niermann, M. Böke, N. Sadeghi, J. Winter, Eur. Phys. J. D. **60**, 489 (2010)

[18] D. Ellerweg, J. Benedikt, A. von Keudell, N. Knake, V. Schulz-von der Gathen, New Journal of Physics **12**, 013021 (2010)

[19] M.J. Kushner, J. Appl. Phys. **95**, 846 (2004)

[20] N.Y. Babaeva, R. Arakoni, M.J. Kushner, J. Appl. Phys. **101**, 123306 (2007)

[21] N.Y. Babaeva, M.J. Kushner, J. Appl. Phys. **101**, 113307 (2007)

[22] N.Y. Babaeva and M. J. Kushner, Plasma Sources Sci. Technol **18**, 035009 (2009)

[23] D.-X. Liu, M.-Z. Rong, X.-H. Wamg, F. Iza, M. Kong, P. Bruggeman, Plasma Process. Polym. **7**, 846 (2010)

[24] M.M. Salem, J.-F. Loiseau, B. Held, Eur. Phys. J - Appl. Phys. **3**, 91 (1998)

[25] D. Ziegler, T. Mussenbrock, R.P. Brinkmann, Plasma Sources Sci. Technol. **17**, 045011 (2008)

[26] V. Léveillé, S. Coulombe, Plasma Process. Polym. **3**, 587 (2006)

[27] J.Y. Jeong, J. Park, I. Henins, S.E. Babayan, V.J. Tu, G.S. Selwyn, G. Ding, R.F. Hicks, J. Phys. Chem. A **104**, 8027 (2000)

[28] A. Fridman, *Plasma Chemistry* (Cambridge University Press, New York, USA, 2008)

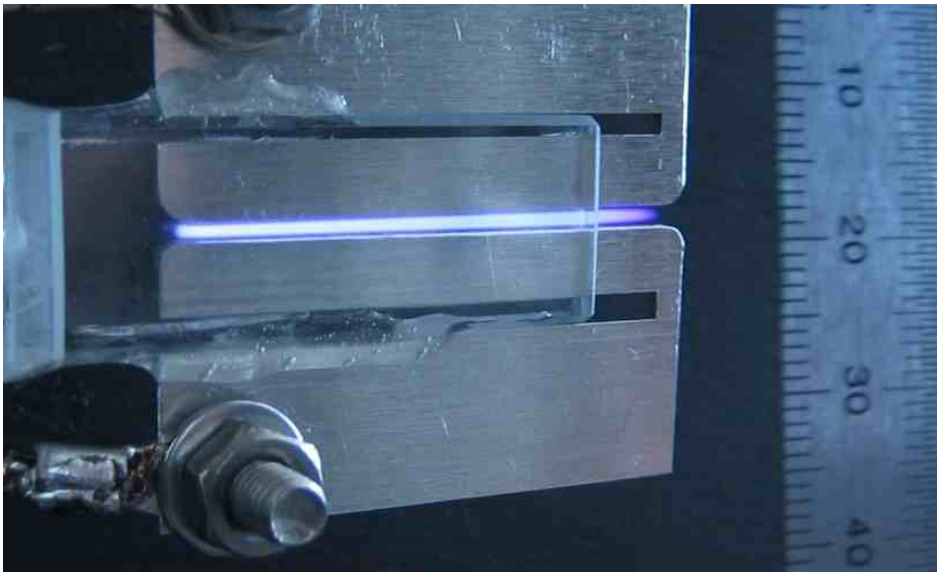

FIG. 1: Photograph of the micro-atmospheric pressure plasma jet (μAPPJ). (Courtesy of Dr. V. Schulz-von der Gathen.) The discharge is confined by the top and bottom electrode and the quartz glasses at the sides of the jet. The stainless steel electrodes are driven at an RF frequency of 13.56 MHz and a nominal power of 10 W. The quartz cuvette allows optical access for diagnostic purposes. The gas mixture is injected in the jet with a high flow rate (left hand side of the jet), while the effluent is formed outside the jet (right hand side of the jet).

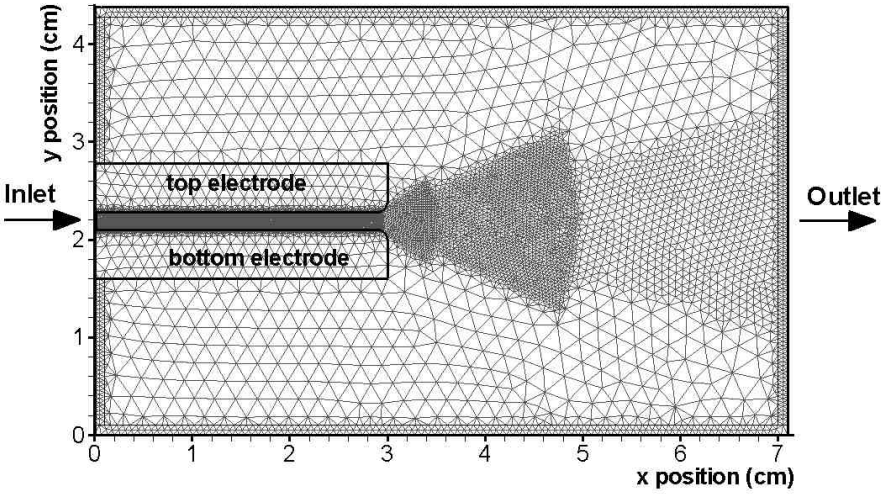

FIG. 2: Simulation domain with numerical mesh. The triangular unstructured mesh consists of approximately 10000 nodes. Around 8000 nodes are located in the plasma region (including the effluent), most of them between the top and bottom electrode. The mesh becomes coarser with increasing distance to the jet nozzle, above and under the electrodes. On the outer border of the simulation domain we employ the Dirichlet boundary condition $\Phi = 0$ for the electrostatic potential (except at the electrodes). We choose an appropriate distance between the electrodes and the boundary to avoid parasitic discharges.

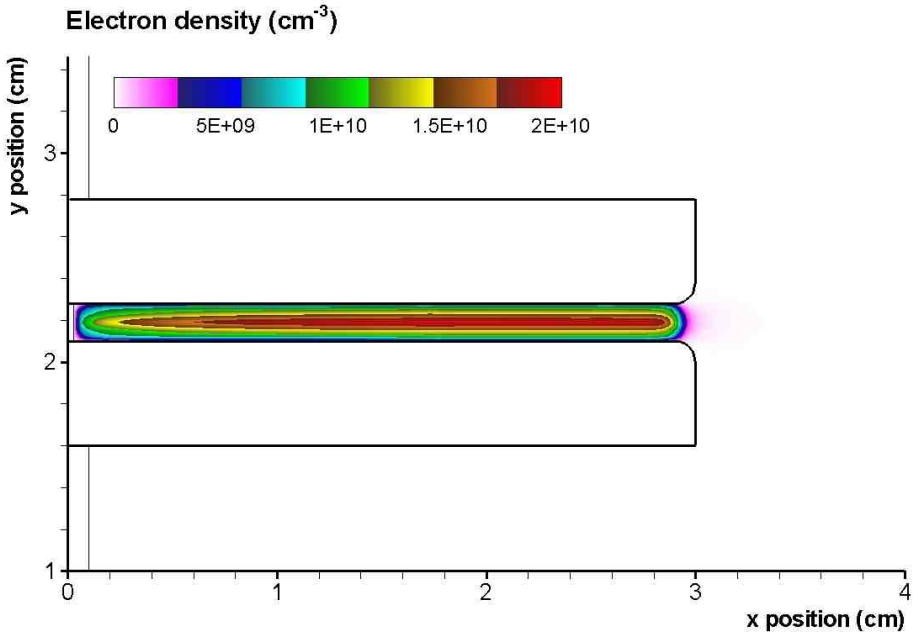

FIG. 3: Spatially resolved electron density n_e averaged over one RF period in units of cm^{-3}. The electron density is confined between the electrodes – it decays rapidly in the effluent.

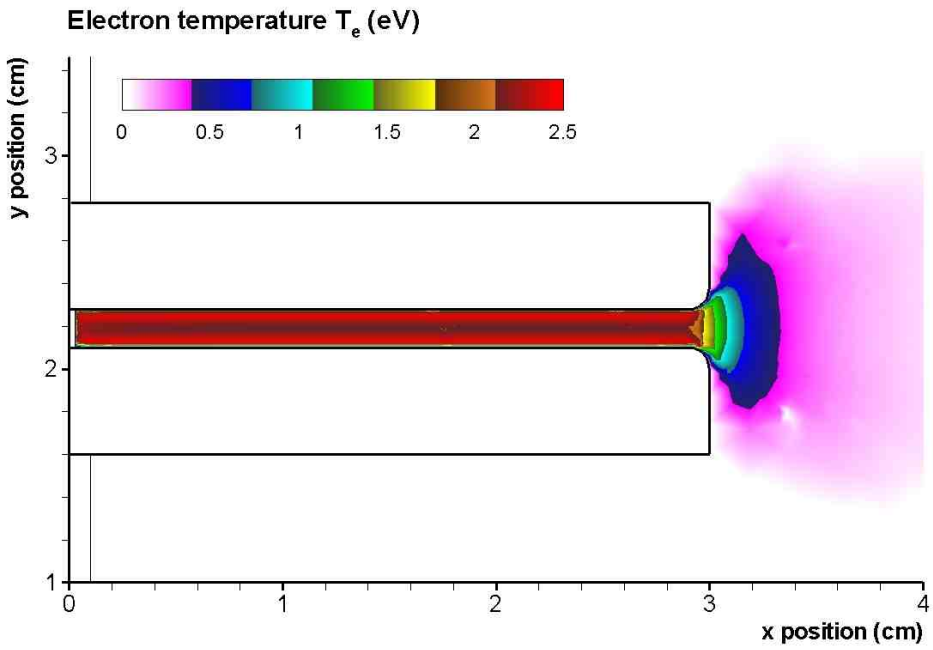

FIG. 4: Spatially resolved electron temperature T_e averaged over one RF period in eV. The electron temperature stays almost constant along the jet channel while decreasing exponentially in the effluent.

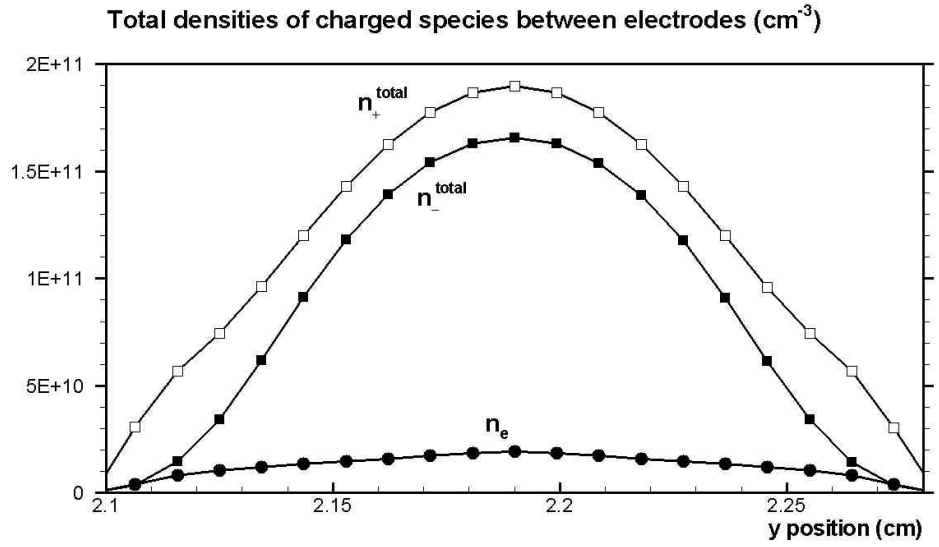

FIG. 5: Densities of charged species (total density of positive ions $n^+_{\rm total}$, negative ions $n^-_{\rm total}$ and electrons e) averaged over one RF period between the electrodes across the jet channel at $x = 2$ cm in units of cm^{-3}. The discharge shows a significant electronegative behavior.

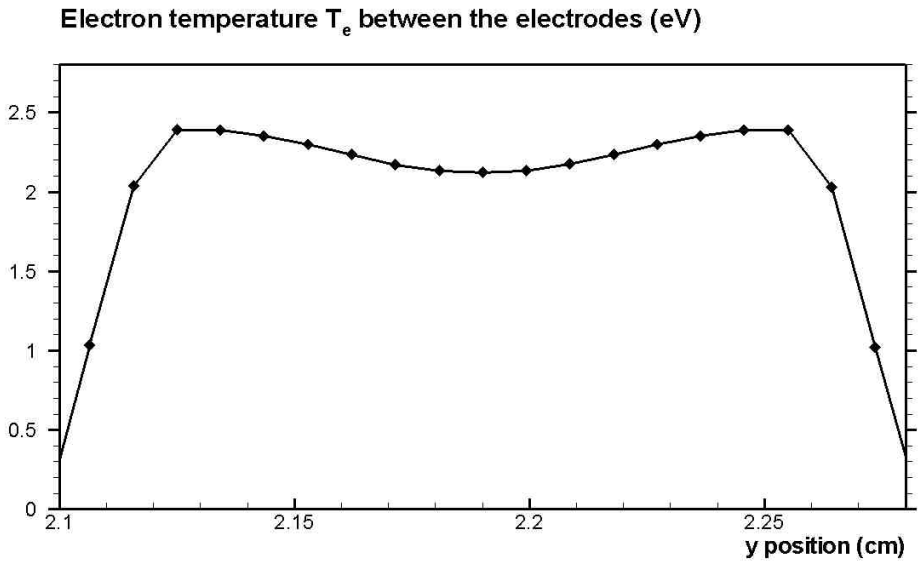

FIG. 6: Electron temperature T_e averaged over one RF period between the electrodes across the jet channel at $x = 2$ cm in units of eV. The maxima of the electron temperature are located at the sheath edge.

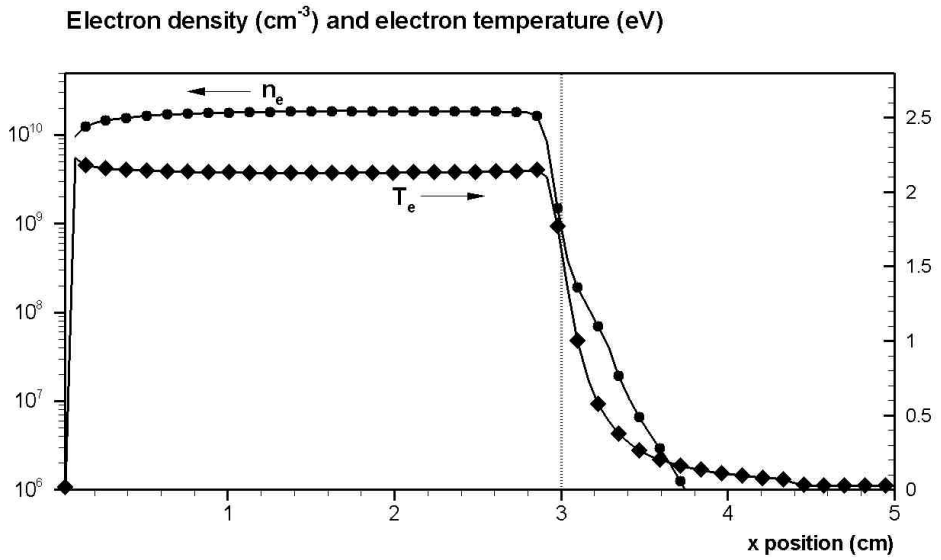

FIG. 7: Electron density (in cm^{-3}) and temperature (in eV) in the center between the electrodes along the jet channel, averaged over one RF period. The vertical dotted line indicates the edge of the electrodes.

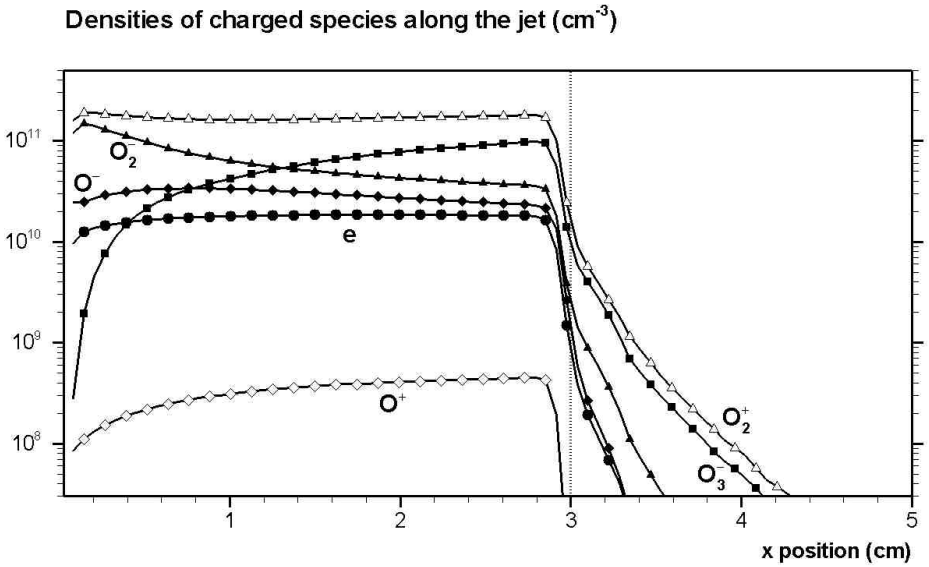

FIG. 8: Logarithmic-linear plot of densities of charged species along the middle axis of the plasma jet. The dotted line at $x = 3$ cm indicates the end of the electrodes of the jet.

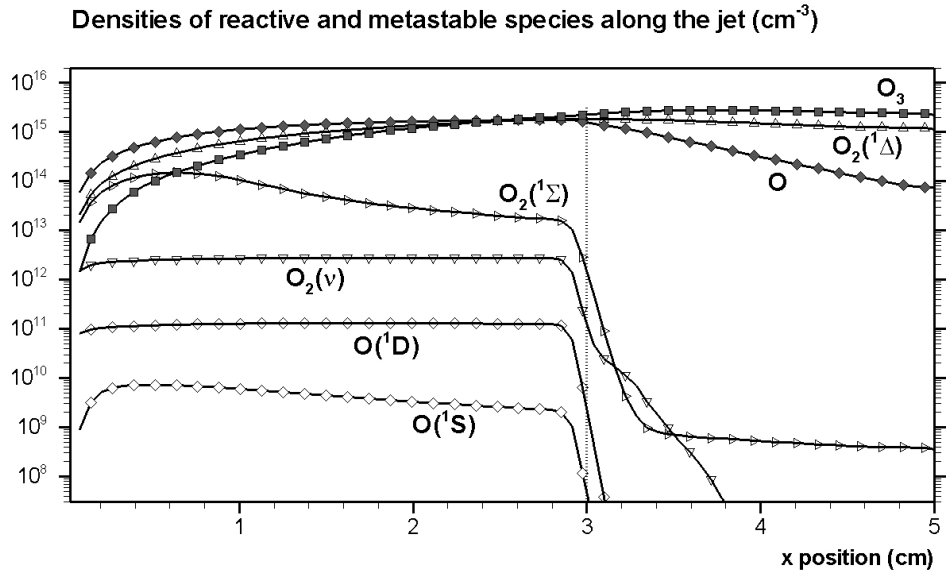

FIG. 9: Logarithmic-linear plot of the reactive species and metastables densities along the middle axis of the plasma jet. The dotted line at $x = 3$ cm indicates the end of the electrodes of the jet.

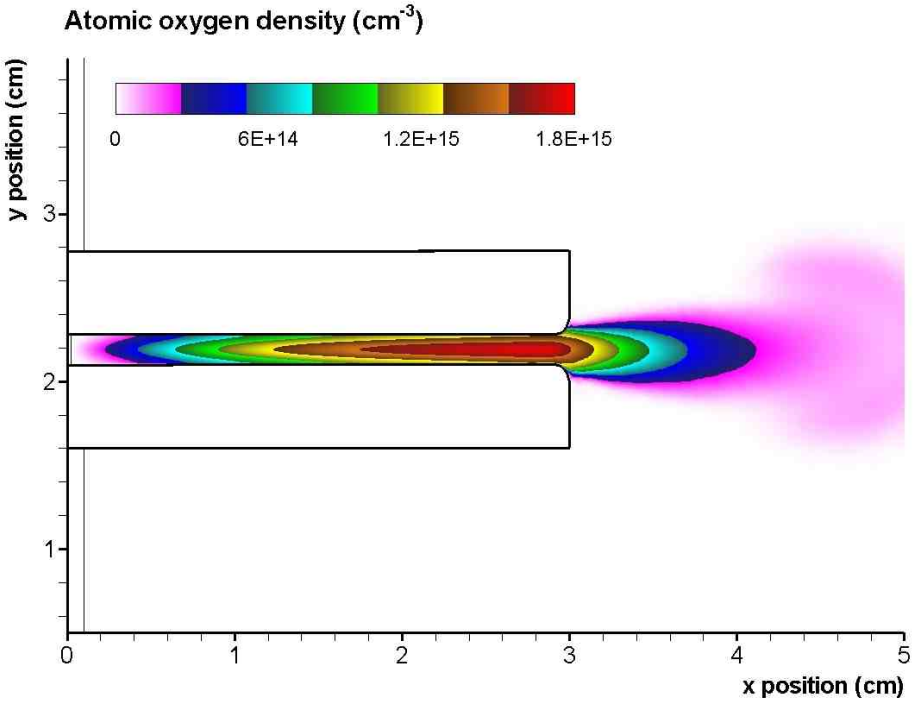

FIG. 10: Spatial distribution of atomic oxygen density in units of cm^{-3}. After reaching the maximum of the concentration at the nozzle of the jet the density decays in the effluent.

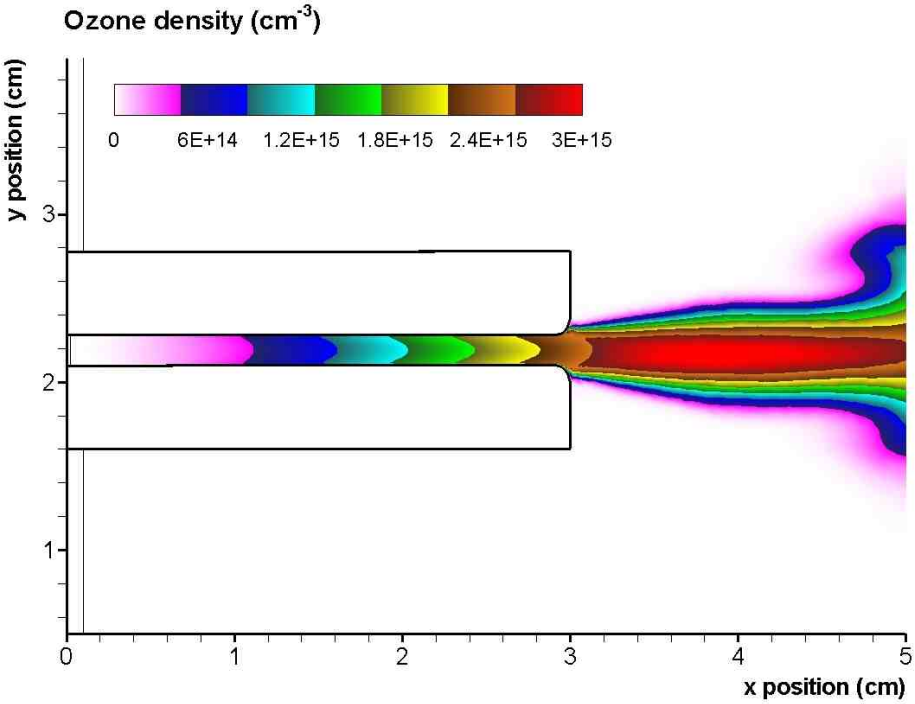

FIG. 11: Spatial distribution of ozone density in units 1of cm^{-3}. The ozone density is nearly constant across the gap and builds up linearly along the flow. A nearly constant level of the ozone concentration maintains in the effluent.

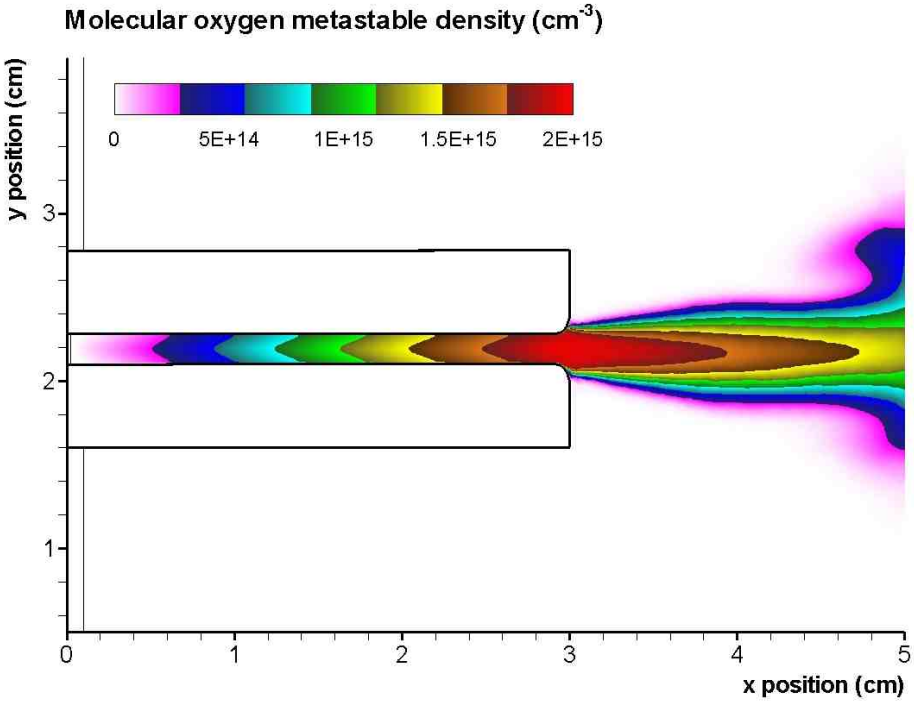

FIG. 12: Spatial distribution of metastable molecular oxygen $O_2(^1\Delta)$ density in units of cm^{-3}. The density of metastable oxygen is nearly constant across the gap and grows linearly with respect to the lateral coordinate x. In the effluent a slow decay is observed.

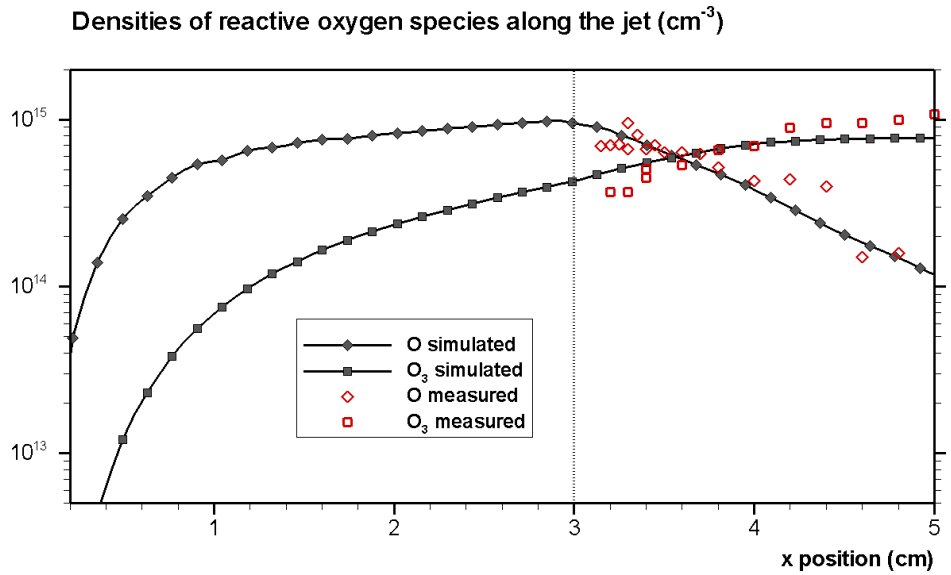

FIG. 13: Comparison of the spatial distribution of the densities of reactive oxygen species in units of cm^{-3} from the simulation with experimental results [18].